

The alignment of galaxies at the Baryon Acoustic Oscillation scale

Dennis van Dompsele, Christos Georgiou,^{*} and Nora Elisa Chisari[†]

*Institute for Theoretical Physics, Utrecht University,
Princetonplein 5, 3584 CC, Utrecht, The Netherlands.*

(Dated: January 12, 2023)

Massive elliptical galaxies align pointing towards each other in the structure of the Universe. Such alignments are well-described at large scales through a linear relation with respect to the tidal field of the large-scale structure. At such scales, galaxy alignments are sensitive to the presence of baryon acoustic oscillations (BAO). The shape of the BAO feature in galaxy alignment correlations differs from the traditional peak in the clustering correlation function. Instead, it appears as a trough feature at the BAO scale. In this work, we show that this feature can be explained by a simple toy model of tidal fields from a spherical shell of matter. This helps give a physical insight for the feature and highlights the need for tailored template-based identification methods for the BAO in alignment statistics. We also discuss the impact of projection baselines and photometric redshift uncertainties for identifying the BAO in intrinsic alignment measurements.

I. INTRODUCTION

Baryon acoustic oscillations (BAO, [1]) are sound waves supported by the plasma present in the Universe before recombination. After the Universe became neutral, these waves could no longer travel and remained frozen at a comoving scale of ~ 150 Mpc. In the late Universe, BAO manifest themselves as a subtle but significant percent-level peak in the auto-correlation function of galaxies or matter. Because they constitute a standard ruler of an absolute distance scale, they are regularly used to probe the expansion of the Universe [2].

Any cosmological observable that correlates with the matter field can have a manifestation of BAO. One such observable beyond galaxy clustering statistics is the alignments of galaxies. Galaxies are known to align themselves radially towards other galaxies [3], and this phenomenon can be described, when the alignment is weak, by a proportional response of the projected shape of a galaxy to the projected tidal field of matter [4]. This model is successful in describing the observed alignments of luminous red galaxies at large-scale from wide surveys [5–9]. Although intrinsic alignments are typically regarded a contaminant to other cosmological observables [3, 10–13], there are examples of how they can be used for extracting cosmological information [14–18].

In principle, a detection of BAO could be achieved in the correlation function of galaxy alignments around other galaxies. In [14], it was shown that such a detection was within the reach of existing surveys. For luminous galaxies in the Baryon Oscillation Spectroscopic Survey (BOSS, [19]), the signal-to-noise ratio (S/N) would be of the order of ~ 2.7 . For upcoming data sets such as the Dark Energy Spectroscopic Instrument (DESI, [20]), the expectation is for this to increase to $S/N \sim 12$.

Searches for BAO in galaxy statistics often adopt matched templates [21, 22], decompositions thereof [23,

24] or remove the smooth (no BAO) component [25]. In [14], it was noticed that the shape of the BAO differs from the traditionally expected ‘peak’ at 150 Mpc. When looking at the alignment of galaxies with the matter field, it rather appears as a trough at a similar distance, followed by a peak at larger comoving separations. This behavior was recently confirmed by [26], who measured the alignment of massive (cluster-scale) halos with the underlying matter field in the DARKQUEST N-body simulations [27]. These authors also pointed out a similar behaviour for the correlation of halo alignments with the velocity field, with the BAO appearing as trough rather than a peak.

In light of possible upcoming detections of this feature, we aim here to give an intuitive physical picture of the origin of this trough pattern rooted in simple linear physics. We show that gravitational tides in and around a spherical shell of matter display exactly the trough pattern and justify its appearance in both matter- and velocity-alignment cross-correlations. We also discuss the impact of long projection baselines and photometric redshifts for identifying the BAO in observational data.

This work is organised as follows. In Section II, we introduce the most widely used linear model for the shapes of galaxies and halos, we present the equations for correlations with matter, galaxies and velocity field, we explain how we model BAO using two approaches which differ in complexity, and how tidal fields are calculated for the simple toy model. Section III gives our results and we conclude in Section IV.

In the matter power spectrum, BAOs appear as a series of successive peaks or ‘wiggles’ at different wavenumbers. In real space, this corresponds to a peak in the three-dimensional correlation function of galaxies, at a comoving scale of ~ 150 Mpc [28]. In this work, we model a Universe with and without BAO ‘wiggles’ using the analytical approximation of [29] for a cosmology with $\sigma_8 = 0.8158$, $h = 0.6774$, $\Omega_m = 0.3089$, $\Omega_b = 0.0486$ and $n_s = 0.9667$, consistent with constraints from the *Planck* satellite [30]. The matter power spectra at $z = 0$ are output by the NBODYKIT software [31]. Other cosmo-

^{*} c.georgiou@uu.nl

[†] n.e.chisari@uu.nl

logical quantities were obtained via the Core Cosmology Library[32] [33]. In the following sections, we compare our predictions for the alignment correlation function for both models.

II. MODELLING

A. Linear alignment model

In the linear alignment model [4], galaxies align their observed two-dimensional shapes proportionally to the projected tidal field of matter. This is mathematically described as:

$$(\gamma_+, \gamma_\times) = -\frac{C_1}{4\pi G}(\partial_x^2 - \partial_y^2, 2\partial_x\partial_y)\phi_p \quad (1)$$

where C_1 is an unknown proportionality constant, i.e. the alignment ‘bias’ and ϕ_p is the primordial gravitational potential (i.e. at some high redshift when the galaxy was formed). This gives a prescription for connecting galaxy shapes to the underlying gravitational potential field and leaves C_1 as a free parameter. As a result, galaxy shapes are expected to be correlated with any observable that depends on the gravitational potential, or the matter field which sources it.

The linear alignment model is known to provide a good description of elliptical galaxies in both simulations [34–37] and observations [5–9] and it is widely used in cosmological studies which aim to extract information from gravitational lensing [e.g. 38–40]. Here, intrinsic alignments act as a contaminant. (We will not cover blue/spiral galaxies in this work, to which different models are thought to apply, namely based on tidal torque theory [41–43].)

In general, the strength (or ‘bias’) of alignment C_1 is constrained from observations [5–9]. We know from them that this constant is generally positive. In this context, this means that elliptical galaxies tend to point radially towards peaks in the density field. [44] proposed a method for estimating C_1 using the stellar distribution function of elliptical galaxies. Using this method, once again one expects that $C_1 > 0$. However, the predicted alignment seemed to fall short of the observed one. This could be a consequence of alignments of galaxies being built-up over time, rather than instantaneously reacting to the tidal field. For our purposes, it suffices to emphasise that the sign of C_1 is at least observationally constrained for elliptical galaxies that are the subject of our work. A completely analogous model and arguments would apply for halos as well, where C_1 is also known to be positive [45].

The most commonly measured statistic of galaxy intrinsic shapes is the projected correlation function of galaxy positions and the + component of the shape, $w_{g+}(r_p)$, which is a function of the projected comoving separation between galaxies. At any given redshift, this is given by an integral along separation in comoving radial distance (Π) of the three-dimensional correlation of positions and shapes, $\xi_{g+}(r_p, \Pi, z)$:

$$w_{g+}(r_p, z) = \int_{-\Pi_{\max}}^{\Pi_{\max}} d\Pi \xi_{g+}(r_p, \Pi, z). \quad (2)$$

Here, ξ_{g+} is defined as:

$$1 + \xi_{g+} = \langle [1 + \delta_g(\mathbf{x}_1)]\gamma_+(\mathbf{x}_2) \rangle, \quad (3)$$

and $\mathbf{r} = \mathbf{x}_2 - \mathbf{x}_1$.

Because galaxy alignments only arise between galaxies that are physically close, Π_{\max} is usually restricted to scales $\lesssim 100 h^{-1}\text{Mpc}$. This justifies assuming a separate dependence of ξ_{g+} on Π and redshift.

In the linear alignment model, $\xi_{g+}(r_p, \Pi)$ is given by

$$\xi_{g+}(r_p, \Pi, z) = \frac{b_g C_1 \rho_{\text{crit}} \Omega_m}{2\pi^2 D(z)} \int_0^\infty dk_z \int_0^\infty dk_\perp \frac{k_\perp^3}{k^2} P(k, z) J_2(k_\perp r_p) \cos(k_z \Pi) \quad (4)$$

where $D(z)$ is the growth function, normalized to $(z+1)D(z) = 1$ during matter domination, $P(k, z)$ is the

matter power spectrum, ρ_{crit} is the critical density today and J_2 is the Bessel function of the first kind of order 2. This results in a projected correlation function

$$w_{g+}(r_p, z) = \frac{b_g C_1 \rho_{\text{crit}} \Omega_m}{\pi^2 D(z)} \int_0^\infty dk_z \int_0^\infty dk_\perp \frac{k_\perp^3}{k^2 k_z} P(k, z) J_2(k_\perp r_p) \sin(k_z \Pi_{\max}) \quad (5)$$

Notice that when $b_g = 1$, w_{g+} reduces to the correlation

between matter and the + component of galaxy shapes,

w_{m+} . For simplicity, we will work with w_{m+} from here on. We also note that in the linear alignment model, $w_{g\times}$ is expected to be zero, and we do not consider it further

$$w_{mm}(r_p, z) = \frac{1}{\pi^2} \int_0^\infty dk_z \int_0^\infty dk_\perp \frac{k_\perp}{k_z} P(k, z) J_0(k_\perp r_p) \sin(k_z \Pi_{\max}). \quad (6)$$

This model was used in forecasts by [14], where it was proposed that a detection of BAO could be achieved in the projected alignment correlation function of galaxies. It is also commonly used in fits to the data [e.g. 5, 7]. However, other works adopt larger projections lengths, effectively taking Π_{\max} to infinity [e.g. 8]. The corresponding projected correlation functions in those cases are

$$w_{mm}(r_p, z) = \int_0^\infty \frac{dk_\perp}{2\pi} k_\perp P(k_\perp, z) J_0(k_\perp r_p), \quad (7)$$

$$w_{m+}(r_p, z) = \tilde{C}_1 \int_0^\infty \frac{dk_\perp}{2\pi} k_\perp P(k_\perp, z) J_2(k_\perp r_p). \quad (8)$$

$$w_{(++,\times\times)}(r_p, z) = \frac{1}{2\pi^2} \left(\frac{C_1 \rho_{\text{crit}} \Omega_m}{D(z)} \right)^2 \int_0^\infty dk_z \int_0^\infty dk_\perp \frac{k_\perp^5}{k^4 k_z} P(k, z) [J_4(k_\perp r_p) \pm J_0(k_\perp r_p)] \sin(k_z \Pi_{\max}). \quad (9)$$

C. Modelling photometric redshifts

The correlation functions presented in the sections above assume precise knowledge of the redshift information of our galaxy samples. This would be the case when data are taken from a spectroscopic survey, but such surveys require a predetermined target selection and long integration times which limit the size of galaxy samples that can be obtained. Photometric surveys can overcome this problem at the cost of significantly reduced accuracy in the determination of redshift information by using band photometry instead of spectra.

The accuracy of the photometric redshifts depend on a number of factors, such as the signal-to-noise of the flux measurement of galaxies and the existence of a representative calibration data-set. There are several techniques that can increase the typical accuracy of photometric redshifts. These include mapping of the galaxy red sequence (limited to intrinsically red galaxies) [46, 47], using machine learning techniques with representative overlapping spectroscopic samples as training set (limited by the training set) [48–50] or using narrow band photometry to resolve more features in a galaxy’s spectral energy distribution (which is more observationally costly compared to broad band photometry) [51, 52]. In light of these techniques, it is interesting to investigate how the projected correlation functions change when the galaxy

in this work.

For comparison, the projected correlation function of the matter field, w_{mm} , is given by

where $\tilde{C}_1 = C_1 \rho_{\text{crit}} \Omega_m / D(z)$ for simplicity. Eq. 8 is derived explicitly in the appendix.

B. Shape-shape correlations

Although more sensitive to shape noise, intrinsic shape auto-correlations have been derived in previous work in the context of the linear alignment model and also detected in spectroscopic survey observations [e.g. 5]. The projected correlation functions for shape-shape correlations take the form

samples used are obtained through photometric data.

To compute the projected correlation functions in this context, we model the impact of redshift uncertainty following [48]. The uncertainty is expressed in the probability density function $p(z|\bar{z})$, where z, \bar{z} is the true and observed redshift of a galaxy, respectively. We choose to model this with a generalized Lorentzian distribution,

$$p(z|\bar{z}) \propto \left(1 + \frac{\Delta z^2}{2as^2} \right)^{-a}, \quad (10)$$

where $\Delta z = (z - \bar{z})/(1 + z)$ and a, s are free parameters. In [53] it was shown that this distribution better describes the probability density function compared to a Gaussian one, especially the long tails away from the mean. We fix $a = 2.613$ as was found in [53] and vary $s \in \{0.0035, 0.015, 0.025\}$ to mimic different photometric redshift precision scenarios. The precision is commonly expressed in terms of the scaled median absolute deviation (SMAD) of Δz , given by $\hat{\sigma}_{\Delta z} = k \cdot \text{MAD}$, where $k \approx 1.4826$ and $p(|\Delta z| \leq \text{MAD}) = 1/2$ (using the fact that the median of (10) is at $\Delta z = 0$). The SMAD is a way to quantify a standard deviation equivalent in the case where the distribution is different than a Gaussian.

Assuming that the line-of-sight separation between two galaxy pairs is small compared to the comoving radial distance of their mean redshift, we can express their true redshifts $z_1 + z_2 = 2z_m$ as $\Pi \approx c(z_1 - z_2)/H(z_m)$. The

matter-matter projected correlation function in the presence of redshift uncertainty can be modelled by

$$w_{\text{mm}}^{\text{phot}}(r_p, z_m) = \int_{-\Pi_{\text{max}}}^{\Pi_{\text{max}}} d\Pi \int_0^\infty \frac{d\ell}{2\pi} J_0(\ell\theta) C_{\text{mm}}(\ell, \bar{z}_1, \bar{z}_2), \quad (11)$$

where $r_p \approx \theta\chi(z_m)$ and C_{mm} is the matter-matter angular power spectrum, computed using $p(z_m|\bar{z}_{1,2})$ for the

redshift distribution of its tracers. In a similar way, one can compute the projected matter-shape and shape-shape correlation functions, using the matter-intrinsic and intrinsic-intrinsic angular power spectra, via

$$w_{\text{m}+}^{\text{phot}}(r_p, z_m) = - \int_{-\Pi_{\text{max}}}^{\Pi_{\text{max}}} d\Pi \int_0^\infty \frac{d\ell}{2\pi} J_2(\ell\theta) C_{\text{mI}}(\ell, \bar{z}_1, \bar{z}_2) \quad (12)$$

and

$$w_{(+,+, \times \times)}^{\text{phot}}(r_p, z_m) = \int_{-\Pi_{\text{max}}}^{\Pi_{\text{max}}} d\Pi \int_0^\infty \frac{d\ell}{2\pi} [J_4(\ell\theta) \pm J_0(\ell\theta)] C_{\Pi}(\ell, \bar{z}_1, \bar{z}_2). \quad (13)$$

D. Correlations with the velocity field

Because intrinsic alignments are correlated with the matter field, we also expect them to be correlated with the velocity field of the large-scale structure [26]. On linear scales, the velocity field and the matter density are related by the continuity equation: $\nabla \cdot \vec{v} = -\delta(1+z)/H(z)f(z)$, where H is the Hubble factor, $f =$

$d \ln D / d \ln a$ is the logarithmic growth rate and \vec{v} is the irrotational velocity field. This leads to a correlation between the divergence of the velocity field and the $+$ component of galaxy shapes. In practice, one expects to actually measure the correlation between projected $+$ shapes and *radial* velocities (along the line-of-sight) [54], which in Fourier space is $v_r \propto (k_z/k)\delta/k$. The w_{v_r+} correlation function is thus modelled by

$$w_{v_r+}(r_p, z) = \frac{C_1 \rho_{\text{crit}} \Omega_m (1+z)}{\pi^2 D(z) H(z) f(z)} \int_0^\infty dk_z \int_0^\infty dk_\perp \frac{k_\perp^3}{k^4} P(k, z) J_2(k_\perp r_p) \sin(k_z \Pi_{\text{max}}). \quad (14)$$

Since the radial velocity field often requires spectroscopic information to be constructed, we do not discuss the effect of photometric redshifts on the w_{v_r+} correlation function (but see [54] for an alternative approach).

E. Tidal field for a spherical mass distribution

To give a qualitative explanation of how the BAO features in the $w_{\text{m}+}$ correlation, we recall that the gravitational potential of a spherical mass distribution is given by

$$\phi(r) = -4\pi G \left[\frac{1}{r} \int_0^r dr_1 \rho(r_1) r_1^2 + \int_r^\infty dr_1 \rho(r_1) r_1 \right]. \quad (15)$$

where $\rho(r_1)$ is the density of matter as a function of radius.

For an extended object, the difference between the force acting at any point and the force acting at the center of mass is the tidal force: $\mathbf{T} = \mathbf{F}(\mathbf{x}) - \mathbf{F}(\mathbf{x}_{\text{CM}})$. A small displacement from the center of mass gives rise to a differential change of the force of $dT_j = \tau_{ij} dx^i$, implicitly summing over i and where $\tau_{ij} = -\partial_i \partial_j \phi$ is the tidal tensor. A spherically symmetric gravitational potential

originates a tidal field given by [55]:

$$\tau_{rr}(r) = -\partial_r^2 \phi(r), \quad (16)$$

$$\tau_{\theta\theta}(r) = \tau_{\phi\phi}(r) = -\partial_r \phi(r)/r. \quad (17)$$

The explicit expression in terms of the density profile of the object is

$$\tau_{rr}(r) = 4\pi G \left[\frac{2}{r^3} \int_0^r dr_1 \rho(r_1) r_1^2 - \rho(r) \right], \quad (18)$$

$$\tau_{\theta\theta}(r) = \tau_{\phi\phi}(r) = \frac{4\pi G}{r^3} \int_0^r dr_1 \rho(r_1) r_1^2, \quad (19)$$

and this can also be expressed in terms of the mean density interior to a given radius, $\bar{\rho}(r)$. For example, as $\tau_{rr}(r) = 4\pi G[2\bar{\rho}(r)/3 - \rho(r)]$.

F. A simple BAO model

We model the BAO as a spherical shell of mass M_{BAO} , with an inner radius R_{BAO} , width ΔR and uniform density ρ_{BAO} . We will neglect the smooth extended component that corresponds to the matter distribution inside and outside the shell, and focus only on how the tidal field changes when the BAO shell is added.

Looking at Figure 1, we first examine the tidal field of the mass configuration on the xy plane. This should be qualitatively representative of the projection along the line of sight, although we will discuss the impact of the projection in more detail below. We imagine taking a

spherical coordinate system where $\phi = 0$ is aligned with the projection (z) axis. According to Eq. 1, we would then have the change in shapes due to the presence of the BAO being $\gamma_+^{\text{BAO}} = C_1[\tau_{rr}(r) - \tau_{\theta\theta}(r)]/(4\pi G)$.

The radial and θ components of the tidal field for such configuration are

$$\tau_{rr}(r) = \begin{cases} 0 & r \leq R_{\text{BAO}} \quad \text{(I)} \\ -4\pi G \rho_{\text{BAO}} [1/3 + 2/3(R_{\text{BAO}}/r)^3] & R_{\text{BAO}} < r \leq R_{\text{BAO}} + \Delta R \quad \text{(II)} \\ 2GM_{\text{BAO}}/r^3 & r > R_{\text{BAO}} + \Delta R \quad \text{(III)} \end{cases} \quad (20)$$

$$\tau_{\theta\theta}(r) = \begin{cases} 0 & r \leq R_{\text{BAO}} \quad \text{(I)} \\ 4\pi G \rho_{\text{BAO}} [1 - (R_{\text{BAO}}/r)^3]/3 & R_{\text{BAO}} < r \leq R_{\text{BAO}} + \Delta R \quad \text{(II)} \\ GM_{\text{BAO}}/(3r^3) & r > R_{\text{BAO}} + \Delta R \quad \text{(III)} \end{cases} \quad (21)$$

respectively, where we have identified three regions of interest: inside the spherical shell (I), within the shell (II) and outside (III). Similarly, $\tau_{\phi\phi}(r) = \tau_{\theta\theta}(r)$.

In addition to this simple model, we also consider a slightly more realistic Gaussian form for the density profile of the shell, with a center at $R_{\text{BAO}} + \Delta R/2$ and a dispersion $\sigma_{\text{BAO}} = \Delta R/2$. We obtain the tidal field in this scenario numerically integrating Eqs. 18 and 19. We then use the change of shapes (γ_+^{BAO}) to explain deviations in w_{mm} from w_{m+} based on the definition given in Eq. 2.

III. RESULTS

Figure 1 illustrates the geometry of the problem. Stacking on as many galaxies as possible and measuring the matter (or galaxy) distribution around them, one would find it slightly enhanced at scales equal to or smaller than the BAO comoving distance scale due to projection over the line-of-sight. The wider the range in Π , the higher the dilution of the BAO peak in projection, and the further in it will move in r_p .

Figure 2 shows the projected matter correlation function (top panel), computed at $z = 0$, for different values of Π_{max} in a universe with and without wiggles. BAO feature as an enhancement of the correlation function at a projected comoving separation of approximately $\sim 110 h^{-1}$ Mpc. Because of projection effects, such a distance is slightly reduced compared to the comoving distance at which one would find the BAO peak for the three-dimensional correlation function of matter. The larger the projection baseline (Π_{max}), the further the peak moves towards smaller separations.

In the bottom panel of Figure 2, we show the projected alignment correlation function, computed at $z = 0$, for different values of Π_{max} in a Universe with and without wiggles. Compared to w_{mm} in the top panel of Figure 2,

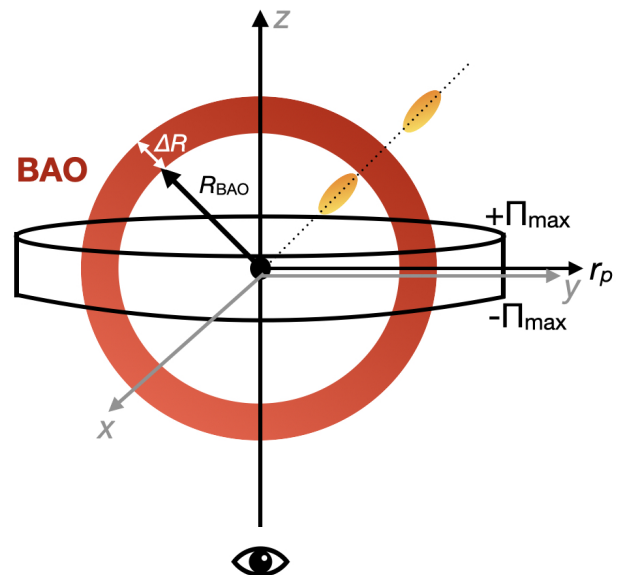


FIG. 1. A sketch showing the geometry of the problem. According to observational constraints on the linear alignment model, galaxies (orange) align themselves radially towards density peaks. These constraints come from integrating the three-dimensional correlation function of galaxy positions and shapes along a line-of-sight baseline of Π_{max} (black cylinder), typically $\lesssim R_{\text{BAO}}$, the BAO scale. The BAO is represented as a spherical shell of matter around the center of the potential. The reader should interpret that the smooth ‘no wiggles’ component has been subtracted in this image.

we see clearly that, at the location of the original BAO peak, there is now a trough, followed by a peak at a larger distance. This is indeed the feature that was seen in previous theoretical predictions and numerical simulations.

To explain why it differs so from w_{mm} , we make the following simplification of the problem: we assume that

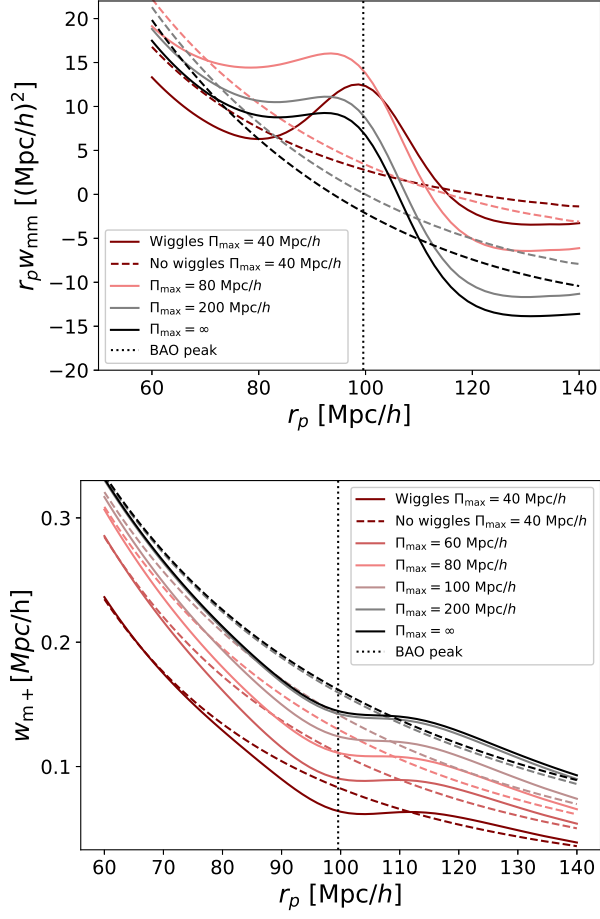


FIG. 2. Projected correlation functions for matter clustering, w_{mm} (top) and alignments of galaxies with the matter field, w_{m+} (bottom), projected over different line-of-sight baselines, $\Pi_{\text{max}} = [40, 60, 80] h^{-1} \text{ Mpc}$, for universes with (solid) and without (dashed) BAO. The BAO peak scale is indicated as a dotted vertical line. This corresponds to a peak in the case of w_{mm} and a trough for w_{m+} .

the BAO is a spherical shell centered at the origin, and that we are interested in computing the tides produced by this shell in the radial direction: τ_{rr} and in the θ direction: $\tau_{\theta\theta}$, according to Eqs. 20 and 21, respectively. This can be combined to predict γ_+^{BAO} . Our assumptions are justified by our findings in Figure 2, in which we see the BAO feature appear as a peak in w_{mm} (top panel).

γ_+^{BAO} is shown in Figure 3. This should be interpreted as the change in the intrinsic shapes of elliptical galaxies from a universe with BAO to a universe without BAO. (For illustration purposes, we adopt here $C_1 = 1$.) It is calculated by fixing the outer rim of the shell to $R_{\text{BAO}} + \Delta R = 150 \text{ Mpc}$ and varying the choice of ΔR . The overall mass normalization, M_{BAO} is arbitrary, but conserved, while varying ΔR . Consistently with Eq. 20 we see that as a result of the BAO matter shell, the tidal field is unchanged inside the shell (Region I: $R < R_{\text{BAO}}$),

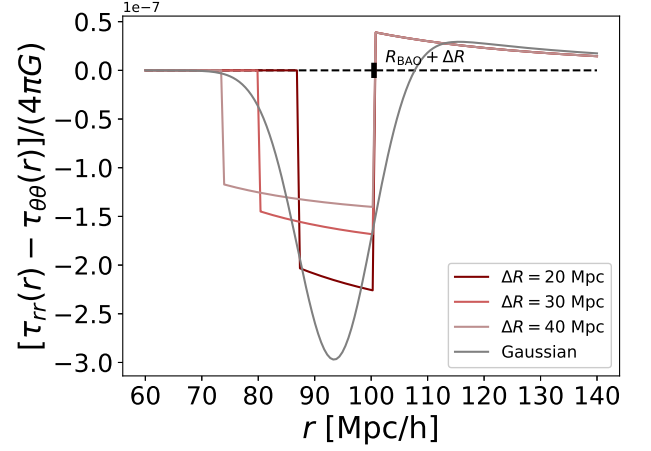


FIG. 3. γ_+^{BAO} given the tidal field (normalized) of a spherical mass shell configuration spanning from R_{BAO} to $R_{\text{BAO}} + \Delta R$ and assuming $C_1 = 1$ for illustration purposes. We plot the function for different BAO widths: $\Delta R = [20, 30, 40] \text{ Mpc}$ in shades of red. In region III, where $r > R_{\text{BAO}} + \Delta R$, the increase in the tidal field is consistent with the addition of a point mass M_{BAO} . In Region II, within the BAO shell, we see a suppression of the tidal field compared to the ‘no wiggles’ case. In Region I, inside the BAO shell, the tidal field remains unchanged. We also plot γ_+^{BAO} as originated from a spherical mass shell with a Gaussian profile centered at $R_{\text{BAO}} + \Delta R/2$ and with a dispersion of $\Delta R/2$ (gray).

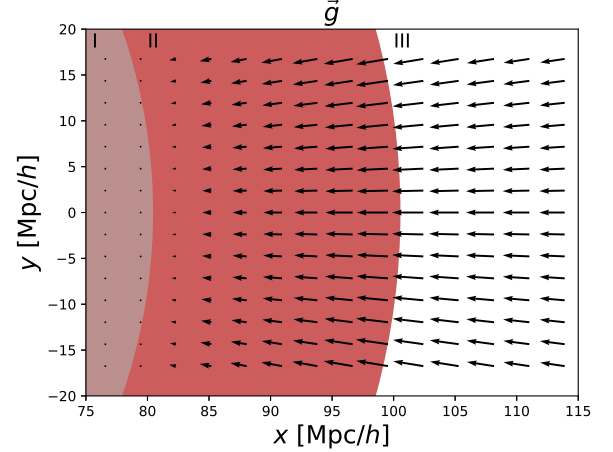


FIG. 4. The gravitational acceleration vector, \vec{g} from a spherical shell of matter. Three regions are indicated: region I inside the shell, region II within the shell and region III outside the shell. There is no gravity in region I. It builds up in region II and is the same as for a point mass with M_{BAO} in region III.

it decreases within the shell and it increases outside of it. The increase is originated by the addition of the mass M_{BAO} , compared to the case where this is absent.

The Gaussian model (gray curve) represents a slightly more realistic situation in which the BAO has no sharp edge. For this case, we only show one possible scenario

with a dispersion which corresponds to 10 Mpc. The behaviour of the curve is similar in general to the hard-edge model, although γ_+^{BAO} transitions from negative to positive values at larger separations, above $R_{\text{BAO}} + \Delta R$.

A model galaxy represented by a sphere embedded in this tidal field is deformed in the following way. Inside the shell, in region I, there is no deformation. Within the shell, in region II, the gravitational force increases with separation. This can be seen in the two-dimensional representation of the gravitational acceleration vector ($\vec{g} = -\nabla\phi$) shown in Figure 4. The tidal field is thus negative in region II and thus compressive along the radial direction. Outside the shell, in region III, tidal forces are positive and thus disruptive, elongating the galaxy along the radial direction. This is due to the gravitational force decreasing outside the shell in the radial direction.

A. Velocity-shape alignments

We also obtained the line-of-sight velocity-intrinsic shape projected correlation function, shown in Figure 5. This shows very similar BAO behaviour to w_{m+} in the right panel of Figure 2. There is trough at the BAO scale, followed by an excess at larger scales compared to the ‘no wiggles’ case. This is justified by the fact that at these scales, the velocity field of the large-scale structure follows the linear continuity equation, resulting in $v(k) \propto \delta(k)/k$. It is thus not surprising that the BAO would also follow qualitatively the tidal field of the spherical shell of mass as presented in Figure 3, confirming the findings of [26].

B. Shape-shape correlations

For completion, we also show in Figure 6 the impact of the BAO feature in shape-shape correlations. BAO appear as a peak in the w_{++} correlation function rather than a trough. The opposite is true for the $w_{\times\times}$ correlation.

C. Long projection baselines and photometric redshifts

The bottom panel of Figure 2 presents w_{m+} integrated over an infinite projection baseline. We see that as Π_{max} increases, BAO become progressively smeared. The evolution of the amplitude of w_{m+} is monotonic and information progressively saturates as $\Pi_{\text{max}} \rightarrow \infty$. In practice, most observational works adopt $60 h^{-1} \text{Mpc} < \Pi_{\text{max}} < 100 h^{-1} \text{Mpc}$. The shape of the BAO is preserved with increasing Π_{max} . This is similar in the case of w_{mm} in the top panel of Figure 2, though here the correlation amplitude does not change monotonically. For all cases, we notice the BAO feature (peak or trough depending on

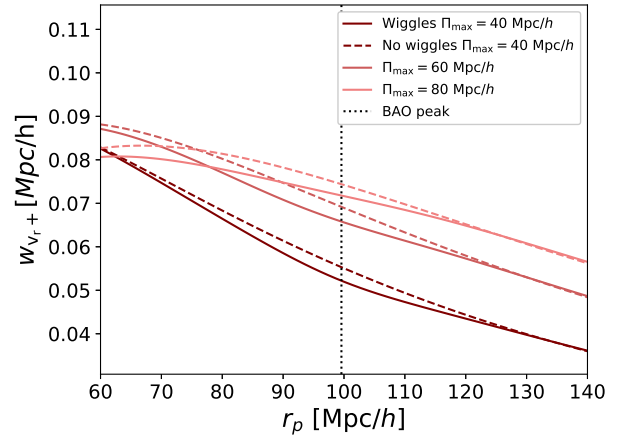


FIG. 5. Projected correlation function for line-of-sight velocity-alignment statistics, w_{v_r+} , projected over different line-of-sight baselines, $\Pi_{\text{max}} = [40, 60, 80] h^{-1} \text{Mpc}$, for universes with (solid) and without (dashed) BAO. The BAO peak scale is indicated by a dotted vertical line. This corresponds to a trough in w_{v_r+} .

the fields considered) move inwards as a consequence of the increased projection length.

Next, we address the impact of redshift uncertainty, such as in the case of photometrically obtained redshift information (photo- z), on the projected correlation functions. We choose three different uncertainty scenarios: redshifts obtained by narrow-band photometry with $\hat{\sigma}_{\Delta z} \sim 0.004$ [52], redshifts obtained over a bright galaxy sample or using the galaxy red sequence with $\hat{\sigma}_{\Delta z} \sim 0.018$ [46, 47, 49] and redshifts obtained from an optimized *gold* sample from large photometric surveys with $\hat{\sigma}_{\Delta z} \sim 0.03$ [50, 56]. The last value is also equal to requirements in the uncertainty of the photo- z scatter for next generation photometric surveys, such as the Vera Rubin Observatory LSST [57].

Figure 7 shows the projected correlation functions w_{mm} , w_{m+} and w_{++} computed at $z = 0.2$, in a universe with and without BAO, for the three different redshift uncertainty scenarios. We see that, as the uncertainty gets larger, the BAO feature is less pronounced for all three functions. The behaviour of the clustering and alignment signals are similar to the case with accurate, spectroscopic redshifts (spec- z).

It is also interesting to compare the projected correlation functions in the case of no redshift uncertainty and an infinite Π_{max} to functions with modelled redshift uncertainty. We show this in Figure 8 where the photo- z signal has $\hat{\sigma}_{\Delta z} \sim 0.018$. The signal obtained through photo- z 's is closer to zero in both the clustering and alignment correlation. Since the clustering signal crosses zero at around 110 Mpc/h, the photometric clustering signal appears simply flatter. In the case of matter-shape correlations, the photo- z signal is about a factor of 2 smaller than the spec- z .

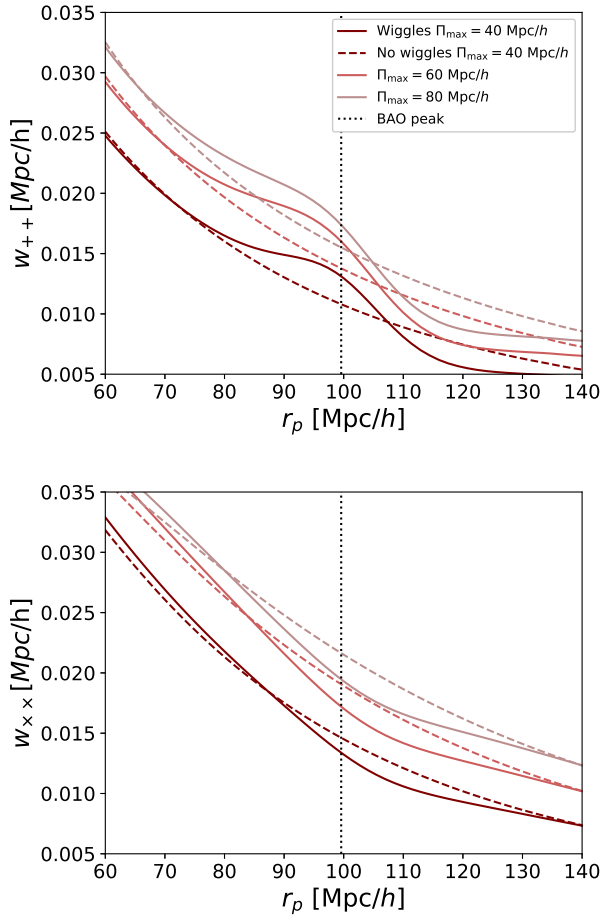


FIG. 6. Projected shape-shape correlation functions for ++ (top) and $\times\times$ (bottom), projected over different line-of-sight baselines, $\Pi_{\max} = [40, 60, 80] h^{-1}$ Mpc, for universes with (solid) and without (dashed) BAO. The BAO peak scale is indicated as a dotted vertical line.

IV. CONCLUSION

While BAO appear as a peak in the matter field projected auto-correlation, in the correlation of matter with intrinsic galaxy shapes, the pattern is replaced by a trough at the same scale, followed by an excess at larger separations. We showed that this behavior is consistent with the response of galaxy shapes to the linear tidal field represented by a shell of matter with radius similar to the location of the BAO peak. A similar behavior is observed for the correlation between intrinsic shapes and radial velocities. Our work highlights the need for dedicated templates for the BAO in such statistic, if a detection is to be attempted. This is, in fact, not far from the reach of current surveys [14].

Progressively increasing projection baselines for the correlation function results in a smearing of the BAO peak. In the case of redshift uncertainty, such as for a sample where the redshift was obtained through photom-

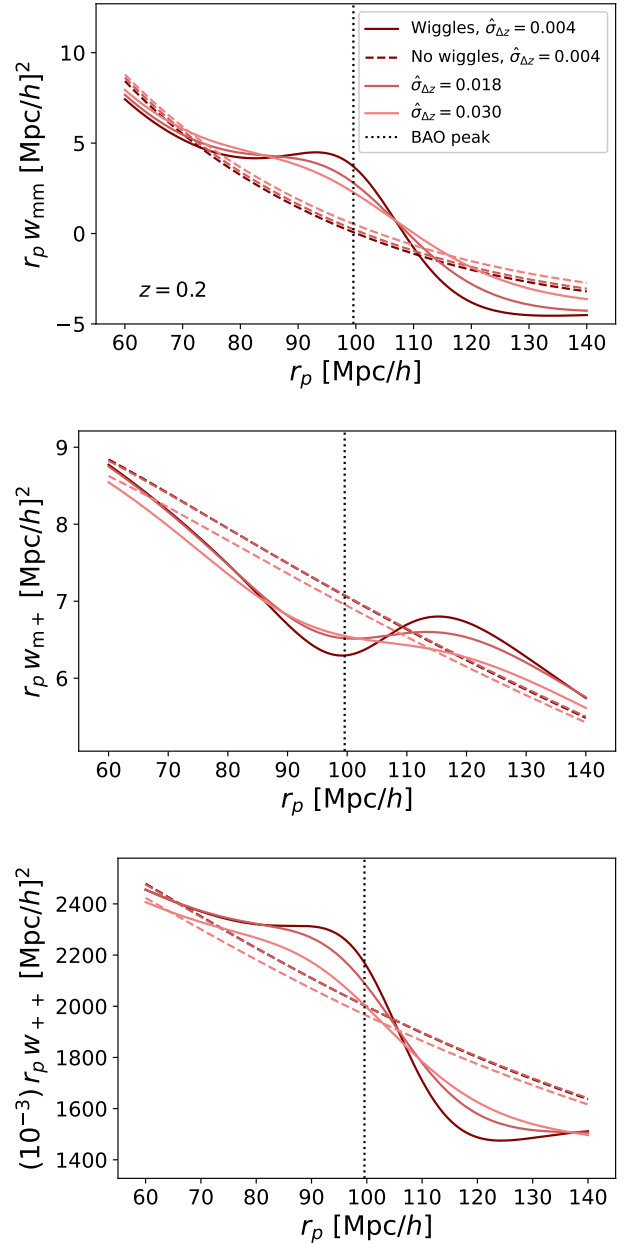


FIG. 7. Projected correlation functions for matter-matter (top), matter-shape (middle) and shape-shape (bottom) correlations computed in the case of redshift uncertainties, quantified by $\hat{\sigma}_{\Delta z} = [0.004, 0.018, 0.3]$, for universes with (solid) and without (dashed) BAO. The BAO peak scale is indicated as a dotted vertical line.

etry, two effects take place in the projected correlation functions. Firstly, the correlation function is closer to zero, meaning the signal is lower. Note, however, that typically large photometric samples are easier to obtain compared to spectroscopic ones. The second effect is that the BAO feature is washed out by the redshift uncertainty. The higher the uncertainty, the less pronounced the BAO feature will be, across all correlation functions.

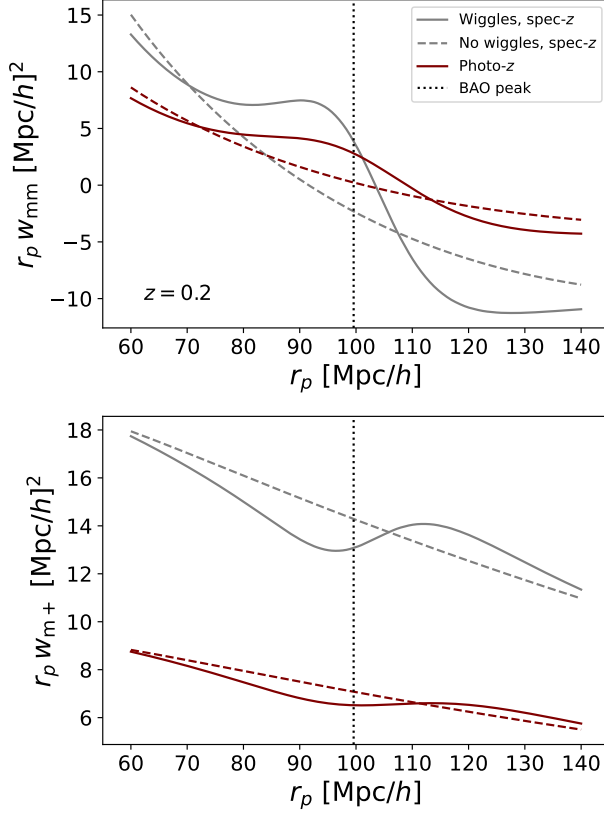


FIG. 8. Projected correlation functions for matter-matter (top) and matter-shape (bottom) correlations computed in the case of accurate, spectroscopic (grey) and photometric (maroon) redshift information, for universes with (solid) and without (dashed) BAO. The BAO peak scale is indicated as a dotted vertical line.

Appendix A: Limber approximation

In this appendix we explicitly show the derivation of Eq. 8 by making use of the Limber approximation [58]. For completeness, we will consider the g+ correlation instead of m+ and we will explicitly model the window functions for the galaxy populations used to trace the density and shape fields. These will be labelled $q_g(\chi) = dN_g/d\chi$ and $q_\gamma(\chi) = dN_\gamma/d\chi$ for number and shape tracers, respectively, and where χ is the comoving line-of-sight distance.

First, we establish that our goal is to calculate Eq. 2 to the case where $\Pi_{\max} \rightarrow \infty$:

$$w_{g+}(r_p) = \int d\chi q_g(\chi) \int d\chi' q_\gamma(\chi') \langle \delta(\vec{x}_p, \chi) \gamma_+(\vec{x}'_p, \chi') \rangle. \quad (\text{A1})$$

The Limber approximation [58] consists of assuming that the galaxy positions and the intrinsic + component of the shape field are uncorrelated unless they are evaluated at the same redshift or line-of-sight distance. In other words, there is a coherence scale [59] over which the correlation is non-zero and this is much smaller than the infinite projection baseline we are using to project ξ_{m+} .

Replacing the three-dimensional correlation function by its Fourier transform, we obtain

$$w_{g+}(r_p) = \int d\chi q_g(\chi) \int d\chi' q_\gamma(\chi') \int \frac{d^3 k}{(2\pi)^3} \int \frac{d^3 k'}{(2\pi)^3} \langle \hat{\delta}(\vec{k}, \chi) \hat{\gamma}_+(\vec{k}', \chi') \rangle e^{-i\vec{k}_\perp \cdot \vec{x}_\perp} e^{-i\vec{k}'_\perp \cdot \vec{x}'_\perp} e^{-ik_z \chi} e^{-ik'_z \chi'}. \quad (\text{A2})$$

Here we have aligned the component of the wavevector that is perpendicular to the line-of-sight with the x axis

ACKNOWLEDGMENTS

This publication is part of the project ‘‘A rising tide: Galaxy intrinsic alignments as a new probe of cosmology and galaxy evolution’’ (with project number VI.Vidi.203.011) of the Talent programme Vidi which is (partly) financed by the Dutch Research Council (NWO). This work is also part of the Delta ITP consortium, a program of the Netherlands Organisation for Scientific Research (NWO) that is funded by the Dutch Ministry of Education, Culture and Science (OCW).

without loss of generality [5]. By explicitly modelling the power spectrum of the density and the shapes, we can write

$$w_{g+}(r_p) = \int d\chi q_g(\chi) \int d\chi' q_\gamma(\chi') \int \frac{d^3k}{(2\pi)^3} \int \frac{d^3k'}{(2\pi)^3} P_{m+}(\vec{k}, z) (2\pi)^3 \delta_D(\vec{k} - \vec{k}') e^{-i\vec{k}_\perp \cdot \vec{x}_\perp} e^{-i\vec{k}'_\perp \cdot \vec{x}'_\perp} e^{-ik_z \chi} e^{-ik'_z \chi'}. \quad (\text{A3})$$

and collapse one of the integrals in wavevector to obtain

$$w_{g+}(r_p) = \int d\chi q_g(\chi) \int d\chi' q_\gamma(\chi') \int \frac{d^3k}{(2\pi)^3} P_{m+}(\vec{k}, z) e^{-i\vec{k}_\perp \cdot (\vec{x}_\perp - \vec{x}'_\perp)} e^{-ik_z \chi} e^{-ik_z \chi'}. \quad (\text{A4})$$

Applying the Limber approximation,

$$w_{g+}(r_p) = \int d\chi q_g(\chi) q_\gamma(\chi) \int d\chi' \int \frac{d^3k}{(2\pi)^3} P_{m+}(\vec{k}, z) e^{-i\vec{k}_\perp \cdot (\vec{x}_\perp - \vec{x}'_\perp)} e^{-ik_z \chi} e^{-ik_z \chi'}. \quad (\text{A5})$$

From here onward, we will assume $q_g(\chi) = q_\gamma(\chi) = \delta_D(\chi)$, which corresponds to correlations are evaluated at $z = 0$ for simplicity. The integral over χ' can now be brought inside, resulting in a Dirac delta over the line-of-sight wavevector:

$$w_{g+}(r_p) = \int \frac{d^3k}{(2\pi)^3} P_{g+}(\vec{k}, z = 0) e^{-i\vec{k}_\perp \cdot (\vec{x}_\perp - \vec{x}'_\perp)} e^{-ik_z \chi} 2\pi \delta_D(k_z). \quad (\text{A6})$$

Before continuing we re-write P_{g+} explicitly:

$$w_{g+}(r_p) = -\frac{C_1 \rho_{\text{crit}} \Omega_m b_g}{D(z)} \int \frac{d^3k}{(2\pi)^3} P(k, z = 0) \frac{k_x^2 - k_y^2}{k^2} e^{-i\vec{k}_\perp \cdot (\vec{x}_\perp - \vec{x}'_\perp)} e^{-ik_z \chi} 2\pi \delta_D(k_z). \quad (\text{A7})$$

where $\vec{k}_\perp = (k_x, k_y)$. The presence of the Dirac delta in k_z simplifies the whole expression to

$$w_{g+}(r_p) = -\frac{C_1 \rho_{\text{crit}} \Omega_m b_g}{D(z)} \int \frac{d^2k_\perp}{(2\pi)^2} P(k_\perp, z = 0) \frac{k_x^2 - k_y^2}{k_\perp^2} e^{-i\vec{k}_\perp \cdot (\vec{x}_\perp - \vec{x}'_\perp)}. \quad (\text{A8})$$

If θ_k is the angle between \vec{k}_\perp and the x axis and $k_\perp = |\vec{k}_\perp|$, then

$$w_{g+}(r_p) = -\frac{C_1 \rho_{\text{crit}} \Omega_m b_g}{D(z)} \int \frac{dk_\perp d\theta_k k_\perp}{(2\pi)^2} P(k_\perp, z = 0) \cos(2\theta_k) e^{-ik_\perp r_p \cos \theta_k}. \quad (\text{A9})$$

This makes the second order Bessel function appear and now the integral is over the absolute value of

$$w_{g+}(r_p) = \frac{C_1 \rho_{\text{crit}} \Omega_m b_g}{D(z)} \int \frac{dk_\perp}{2\pi} k_\perp P(k_\perp, z) J_2(k_\perp r_p). \quad (\text{A10})$$

Similarly for the correlation with the matter field,

$$w_{m+}(r_p) = \frac{C_1 \rho_{\text{crit}} \Omega_m}{D(z)} \int \frac{dk_\perp}{2\pi} k_\perp P(k_\perp, z) J_2(k_\perp r_p). \quad (\text{A11})$$

This is in agreement with Eq. 8.

[1] B. Bassett and R. Hlozek, Baryon acoustic oscillations, in *Dark Energy: Observational and Theoretical Approaches*, edited by P. Ruiz-Lapuente (2010) p. 246.

[2] D. H. Weinberg, M. J. Mortonson, D. J. Eisenstein, C. Hirata, A. G. Riess, and E. Rozo, Observational probes of cosmic acceleration, *Phys. Rep.* **530**, 87 (2013), arXiv:1201.2434 [astro-ph.CO].

[3] M. L. Brown, A. N. Taylor, N. C. Hambly, and S. Dye, Measurement of intrinsic alignments in galaxy ellipticities, *MNRAS* **333**, 501 (2002), arXiv:astro-ph/0009499 [astro-ph].

[4] P. Catelan, M. Kamionkowski, and R. D. Blandford, Intrinsic and extrinsic galaxy alignment, *MNRAS* **320**, L7 (2001), arXiv:astro-ph/0005470 [astro-ph].

- [5] J. Blazek, M. McQuinn, and U. Seljak, Testing the tidal alignment model of galaxy intrinsic alignment, *J. Cosmology Astropart. Phys.* **2011**, 010 (2011), arXiv:1101.4017 [astro-ph.CO].
- [6] B. Joachimi, R. Mandelbaum, F. B. Abdalla, and S. L. Bridle, Constraints on intrinsic alignment contamination of weak lensing surveys using the MegaZ-LRG sample, *A&A* **527**, A26 (2011), arXiv:1008.3491 [astro-ph.CO].
- [7] S. Singh, R. Mandelbaum, and S. More, Intrinsic alignments of SDSS-III BOSS LOWZ sample galaxies, *MNRAS* **450**, 2195 (2015), arXiv:1411.1755 [astro-ph.CO].
- [8] H. Johnston, C. Georgiou, B. Joachimi, H. Hoekstra, N. E. Chisari, D. Farrow, M. C. Fortuna, C. Heymans, S. Joudaki, K. Kuijken, and A. Wright, KiDS+GAMA: Intrinsic alignment model constraints for current and future weak lensing cosmology, *A&A* **624**, A30 (2019), arXiv:1811.09598 [astro-ph.CO].
- [9] M. C. Fortuna, H. Hoekstra, H. Johnston, M. Vakili, A. Kannawadi, C. Georgiou, B. Joachimi, A. H. Wright, M. Asgari, M. Bilicki, C. Heymans, H. Hildebrandt, K. Kuijken, and M. Von Wietersheim-Kramsta, KiDS-1000: Constraints on the intrinsic alignment of luminous red galaxies, *A&A* **654**, A76 (2021), arXiv:2109.02556 [astro-ph.CO].
- [10] C. M. Hirata, Tidal alignments as a contaminant of redshift space distortions, *MNRAS* **399**, 1074 (2009), arXiv:0903.4929 [astro-ph.CO].
- [11] D. Kirk, A. Rassat, O. Host, and S. Bridle, The cosmological impact of intrinsic alignment model choice for cosmic shear, *MNRAS* **424**, 1647 (2012), arXiv:1112.4752 [astro-ph.CO].
- [12] E. Krause, T. Eifler, and J. Blazek, The impact of intrinsic alignment on current and future cosmic shear surveys, *MNRAS* **456**, 207 (2016), arXiv:1506.08730 [astro-ph.CO].
- [13] K. Zwetsloot and N. E. Chisari, Impact of intrinsic alignments on clustering constraints of the growth rate, *MNRAS* **516**, 787 (2022), arXiv:2208.07062 [astro-ph.CO].
- [14] N. E. Chisari and C. Dvorkin, Cosmological information in the intrinsic alignments of luminous red galaxies, *J. Cosmology Astropart. Phys.* **2013**, 029 (2013), arXiv:1308.5972 [astro-ph.CO].
- [15] N. E. Chisari, C. Dvorkin, and F. Schmidt, Can weak lensing surveys confirm BICEP2?, *Phys. Rev. D* **90**, 043527 (2014), arXiv:1406.4871 [astro-ph.CO].
- [16] F. Schmidt, N. E. Chisari, and C. Dvorkin, Imprint of inflation on galaxy shape correlations, *J. Cosmology Astropart. Phys.* **2015**, 032 (2015), arXiv:1506.02671 [astro-ph.CO].
- [17] M. Biagetti and G. Orlando, Primordial gravitational waves from galaxy intrinsic alignments, *J. Cosmology Astropart. Phys.* **2020**, 005 (2020), arXiv:2001.05930 [astro-ph.CO].
- [18] A. Taruya and T. Okumura, Improving Geometric and Dynamical Constraints on Cosmology with Intrinsic Alignments of Galaxies, *ApJ* **891**, L42 (2020), arXiv:2001.05962 [astro-ph.CO].
- [19] K. S. Dawson, D. J. Schlegel, C. P. Ahn, S. F. Anderson, É. Aubourg, S. Bailey, R. H. Barkhouser, J. E. Bautista, A. Beifiori, A. A. Berlind, V. Bhardwaj, D. Bizyaev, C. H. Blake, M. R. Blanton, M. Blomqvist, *et al.*, The Baryon Oscillation Spectroscopic Survey of SDSS-III, *AJ* **145**, 10 (2013), arXiv:1208.0022 [astro-ph.CO].
- [20] DESI Collaboration, A. Aghamousa, J. Aguilar, S. Ahlen, S. Alam, L. E. Allen, C. Allende Prieto, J. Annis, S. Bailey, C. Balland, O. Ballester, C. Baltay, L. Beaufore, C. Bebek, T. C. Beers, E. F. Bell, *et al.*, The DESI Experiment Part I: Science, Targeting, and Survey Design, arXiv e-prints, arXiv:1611.00036 (2016), arXiv:1611.00036 [astro-ph.IM].
- [21] H.-J. Seo and D. J. Eisenstein, Improved Forecasts for the Baryon Acoustic Oscillations and Cosmological Distance Scale, *ApJ* **665**, 14 (2007), arXiv:astro-ph/0701079 [astro-ph].
- [22] H.-J. Seo, J. Eckel, D. J. Eisenstein, K. Mehta, M. Metchnik, N. Padmanabhan, P. Pinto, R. Takahashi, M. White, and X. Xu, High-precision Predictions for the Acoustic Scale in the Nonlinear Regime, *ApJ* **720**, 1650 (2010), arXiv:0910.5005 [astro-ph.CO].
- [23] P. Arnalte-Mur, A. Labatie, N. Clerc, V. J. Martínez, J. L. Starck, M. Lachièze-Rey, E. Saar, and S. Paredes, Wavelet analysis of baryon acoustic structures in the galaxy distribution, *A&A* **542**, A34 (2012), arXiv:1101.1911 [astro-ph.CO].
- [24] H. J. Tian, M. C. Neyrinck, T. Budavári, and A. S. Szalay, Redshift-space Enhancement of Line-of-sight Baryon Acoustic Oscillations in the Sloan Digital Sky Survey Main-galaxy Sample, *ApJ* **728**, 34 (2011), arXiv:1011.2481 [astro-ph.CO].
- [25] W. J. Percival, S. Cole, D. J. Eisenstein, R. C. Nichol, J. A. Peacock, A. C. Pope, and A. S. Szalay, Measuring the Baryon Acoustic Oscillation scale using the Sloan Digital Sky Survey and 2dF Galaxy Redshift Survey, *MNRAS* **381**, 1053 (2007), arXiv:0705.3323 [astro-ph].
- [26] T. Okumura, A. Taruya, and T. Nishimichi, Intrinsic alignment statistics of density and velocity fields at large scales: Formulation, modeling, and baryon acoustic oscillation features, *Phys. Rev. D* **100**, 103507 (2019), arXiv:1907.00750 [astro-ph.CO].
- [27] T. Nishimichi, M. Takada, R. Takahashi, K. Osato, M. Shirasaki, T. Oogi, H. Miyatake, M. Oguri, R. Murata, Y. Kobayashi, and N. Yoshida, Dark Quest. I. Fast and Accurate Emulation of Halo Clustering Statistics and Its Application to Galaxy Clustering, *ApJ* **884**, 29 (2019), arXiv:1811.09504 [astro-ph.CO].
- [28] E. Komatsu, J. Dunkley, M. R. Nolte, C. L. Bennett, B. Gold, G. Hinshaw, N. Jarosik, D. Larson, M. Limon, L. Page, D. N. Spergel, M. Halpern, R. S. Hill, A. Kogut, S. S. Meyer, *et al.*, Five-Year Wilkinson Microwave Anisotropy Probe Observations: Cosmological Interpretation, *ApJS* **180**, 330 (2009), arXiv:0803.0547 [astro-ph].
- [29] D. J. Eisenstein and W. Hu, Baryonic Features in the Matter Transfer Function, *ApJ* **496**, 605 (1998), arXiv:astro-ph/9709112 [astro-ph].
- [30] Planck Collaboration, P. A. R. Ade, N. Aghanim, M. Arnaud, M. Ashdown, J. Aumont, C. Baccigalupi, A. J. Banday, R. B. Barreiro, J. G. Bartlett, N. Bartolo, E. Battaner, R. Battye, K. Benabed, A. Benoît, A. Benoit-Lévy, *et al.*, Planck 2015 results. XIII. Cosmological parameters, *A&A* **594**, A13 (2016), arXiv:1502.01589 [astro-ph.CO].
- [31] N. Hand, Y. Feng, F. Beutler, Y. Li, C. Modi, U. Seljak, and Z. Slepian, nbbodykit: An Open-source, Massively Parallel Toolkit for Large-scale Structure, *AJ* **156**, 160 (2018), arXiv:1712.05834 [astro-ph.IM].
- [32] <https://github.com/LSSTDESC/CCL>.

- [33] N. E. Chisari, D. Alonso, E. Krause, C. D. Leonard, P. Bull, J. Neveu, A. S. Villarreal, S. Singh, T. McClintock, J. Ellison, Z. Du, J. Zuntz, A. Mead, S. Joudaki, C. S. Lorenz, T. Tröster, J. Sanchez, F. Lanusse, M. Ishak, R. Hlozek, J. Blazek, J.-E. Campagne, H. Almoubayyed, T. Eifler, M. Kirby, D. Kirkby, S. Plaszczyński, A. Slosar, M. Vrstil, E. L. Wagoner, and LSST Dark Energy Science Collaboration, Core Cosmology Library: Precision Cosmological Predictions for LSST, *ApJS* **242**, 2 (2019), arXiv:1812.05995 [astro-ph.CO].
- [34] A. Tenneti, S. Singh, R. Mandelbaum, T. di Matteo, Y. Feng, and N. Khandai, Intrinsic alignments of galaxies in the MassiveBlack-II simulation: analysis of two-point statistics, *MNRAS* **448**, 3522 (2015), arXiv:1409.7297 [astro-ph.CO].
- [35] N. Chisari, S. Codis, C. Laigle, Y. Dubois, C. Pichon, J. Devriendt, A. Slyz, L. Miller, R. Gavazzi, and K. Benabed, Intrinsic alignments of galaxies in the Horizon-AGN cosmological hydrodynamical simulation, *MNRAS* **454**, 2736 (2015), arXiv:1507.07843 [astro-ph.CO].
- [36] N. Chisari, C. Laigle, S. Codis, Y. Dubois, J. Devriendt, L. Miller, K. Benabed, A. Slyz, R. Gavazzi, and C. Pichon, Redshift and luminosity evolution of the intrinsic alignments of galaxies in Horizon-AGN, *MNRAS* **461**, 2702 (2016), arXiv:1602.08373 [astro-ph.CO].
- [37] S. Hilbert, D. Xu, P. Schneider, V. Springel, M. Vogelsberger, and L. Hernquist, Intrinsic alignments of galaxies in the Illustris simulation, *MNRAS* **468**, 790 (2017), arXiv:1606.03216 [astro-ph.CO].
- [38] C. Hikage, M. Oguri, T. Hamana, S. More, R. Mandelbaum, M. Takada, F. Köhlinger, H. Miyatake, A. J. Nishizawa, H. Aihara, R. Armstrong, J. Bosch, J. Coupon, A. Ducout, P. Ho, *et al.*, Cosmology from cosmic shear power spectra with Subaru Hyper Suprime-Cam first-year data, *PASJ* **71**, 43 (2019), arXiv:1809.09148 [astro-ph.CO].
- [39] C. Heymans, T. Tröster, M. Asgari, C. Blake, H. Hildebrandt, B. Joachimi, K. Kuijken, C.-A. Lin, A. G. Sánchez, J. L. van den Busch, A. H. Wright, A. Amon, M. Bilicki, J. de Jong, M. Crocce, *et al.*, KiDS-1000 Cosmology: Multi-probe weak gravitational lensing and spectroscopic galaxy clustering constraints, *A&A* **646**, A140 (2021), arXiv:2007.15632 [astro-ph.CO].
- [40] L. F. Secco, S. Samuroff, E. Krause, B. Jain, J. Blazek, M. Raveri, A. Campos, A. Amon, A. Chen, C. Doux, A. Choi, D. Gruen, G. M. Bernstein, C. Chang, J. DeRose, DES Collaboration, *et al.*, Dark Energy Survey Year 3 results: Cosmology from cosmic shear and robustness to modeling uncertainty, *Phys. Rev. D* **105**, 023515 (2022), arXiv:2105.13544 [astro-ph.CO].
- [41] C. Porciani, A. Dekel, and Y. Hoffman, Testing tidal-torque theory - I. Spin amplitude and direction, *MNRAS* **332**, 325 (2002), arXiv:astro-ph/0105123 [astro-ph].
- [42] C. Porciani, A. Dekel, and Y. Hoffman, Testing tidal-torque theory - II. Alignment of inertia and shear and the characteristics of protohaloes, *MNRAS* **332**, 339 (2002), arXiv:astro-ph/0105165 [astro-ph].
- [43] S. Codis, C. Pichon, and D. Pogosyan, Spin alignments within the cosmic web: a theory of constrained tidal torques near filaments, *MNRAS* **452**, 3369 (2015), arXiv:1504.06073 [astro-ph.CO].
- [44] G. Camello and M. Lombardi, On the origin of intrinsic alignment in cosmic shear measurements: an analytic argument, *A&A* **575**, A113 (2015), arXiv:1501.03014 [astro-ph.CO].
- [45] E. van Uitert and B. Joachimi, Intrinsic alignment of redMaPPer clusters: cluster shape-matter density correlation, *MNRAS* **468**, 4502 (2017), arXiv:1701.02307 [astro-ph.CO].
- [46] E. Rozo, E. S. Rykoff, A. Abate, C. Bonnett, M. Crocce, C. Davis, B. Hoyle, B. Leistedt, H. V. Peiris, R. H. Wechsler, T. Abbott, F. B. Abdalla, M. Banerji, A. H. Bauer, A. Benoit-Lévy, *et al.*, redMaGiC: selecting luminous red galaxies from the DES Science Verification data, *MNRAS* **461**, 1431 (2016), arXiv:1507.05460 [astro-ph.IM].
- [47] M. Vakili, M. Bilicki, H. Hoekstra, N. E. Chisari, M. J. I. Brown, C. Georgiou, A. Kannawadi, K. Kuijken, and A. H. Wright, Luminous red galaxies in the Kilo-Degree Survey: selection with broad-band photometry and weak lensing measurements, *MNRAS* **487**, 3715 (2019), arXiv:1811.02518 [astro-ph.CO].
- [48] B. Joachimi, R. Mandelbaum, F. B. Abdalla, and S. L. Bridle, Constraints on intrinsic alignment contamination of weak lensing surveys using the MegaZ-LRG sample, *A&A* **527**, A26 (2011), arXiv:1008.3491 [astro-ph.CO].
- [49] M. Bilicki, H. Hoekstra, M. J. I. Brown, V. Amaro, C. Blake, S. Cavuoti, J. T. A. de Jong, C. Georgiou, H. Hildebrandt, C. Wolf, A. Amon, M. Brescia, S. Brough, M. V. Costa-Duarte, T. Erben, *et al.*, Photometric redshifts for the Kilo-Degree Survey. Machine-learning analysis with artificial neural networks, *A&A* **616**, A69 (2018), arXiv:1709.04205 [astro-ph.CO].
- [50] A. H. Wright, H. Hildebrandt, J. L. van den Busch, and C. Heymans, Photometric redshift calibration with self-organising maps, *A&A* **637**, A100 (2020), arXiv:1909.09632 [astro-ph.CO].
- [51] O. Ilbert, P. Capak, M. Salvato, H. Aussel, H. J. McCracken, D. B. Sanders, N. Scoville, J. Kartaltepe, S. Arnouts, E. Le Floc'h, B. Mobasher, Y. Taniguchi, F. Lamareille, A. Leauthaud, S. Sasaki, *et al.*, Cosmos Photometric Redshifts with 30-Bands for 2-deg², *ApJ* **690**, 1236 (2009), arXiv:0809.2101 [astro-ph].
- [52] M. Eriksen, A. Alarcon, E. Gaztanaga, A. Amara, L. Cabayol, J. Carretero, F. J. Castander, M. Crocce, M. Delfino, J. De Vicente, E. Fernandez, P. Fosalba, J. Garcia-Bellido, H. Hildebrandt, H. Hoekstra, *et al.*, The PAU Survey: early demonstration of photometric redshift performance in the COSMOS field, *MNRAS* **484**, 4200 (2019), arXiv:1809.04375 [astro-ph.GA].
- [53] M. Bilicki, A. Dvornik, H. Hoekstra, A. H. Wright, N. E. Chisari, M. Vakili, M. Asgari, B. Giblin, C. Heymans, H. Hildebrandt, B. W. Holwerda, A. Hopkins, H. Johnston, A. Kannawadi, K. Kuijken, *et al.*, Bright galaxy sample in the Kilo-Degree Survey Data Release 4. Selection, photometric redshifts, and physical properties, *A&A* **653**, A82 (2021), arXiv:2101.06010 [astro-ph.GA].
- [54] I. R. van Gemen and N. E. Chisari, Erratum: Prospects for detection and application of the alignment of galaxies with the large-scale velocity field [*Phys. Rev. D* **102**, 123507 (2020)], *Phys. Rev. D* **104**, 069902 (2021), arXiv:2011.07087 [astro-ph.CO].
- [55] M. Masi, On compressive radial tidal forces, *American Journal of Physics* **75**, 116 (2007), arXiv:0705.3747 [astro-ph].
- [56] A. Carnero Rosell, M. Rodriguez-Monroy, M. Crocce, J. Elvin-Poole, A. Porredon, I. Ferrero, J. Mena-Fernández, R. Cawthon, J. De Vicente, E. Gaztanaga, A. J. Ross, E. Sanchez, I. Sevilla-Noarbe, O. Alves,

- F. Andrade-Oliveira, DES Collaboration, *et al.*, Dark Energy Survey Year 3 results: galaxy sample for BAO measurement, *MNRAS* **509**, 778 (2022), arXiv:2107.05477 [astro-ph.CO].
- [57] The LSST Dark Energy Science Collaboration, R. Mandelbaum, T. Eifler, R. Hložek, T. Collett, E. Gawiser, D. Scolnic, D. Alonso, H. Awan, R. Biswas, J. Blazek, P. Burchat, N. E. Chisari, I. Dell’Antonio, S. Digel, J. Frieman, D. A. Goldstein, I. Hook, Ž. Ivezić, S. M. Kahn, S. Kamath, D. Kirkby, T. Kitching, E. Krause, P.-F. Leget, P. J. Marshall, J. Meyers, H. Miyatake, J. A. Newman, R. Nichol, E. Rykoff, F. J. Sanchez, A. Slosar, M. Sullivan, and M. A. Troxel, The LSST Dark Energy Science Collaboration (DESC) Science Requirements Document, arXiv e-prints , arXiv:1809.01669 (2018), arXiv:1809.01669 [astro-ph.CO].
- [58] D. N. Limber, The Analysis of Counts of the Extragalactic Nebulae in Terms of a Fluctuating Density Field., *ApJ* **117**, 134 (1953).
- [59] M. Bartelmann and P. Schneider, Weak gravitational lensing, *Phys. Rep.* **340**, 291 (2001), arXiv:astro-ph/9912508 [astro-ph].